

1

2 **“Improved moist-convective rotating shallow water model and its**

3 **application to instabilities of hurricane-like vortices”**

4 **MASOUD ROSTAMI[†] * and VLADIMIR ZEITLIN[†]**

5 [†] Laboratoire de Météorologie Dynamique/Université Pierre et Marie Curie (UPMC)/ Ecole Normale Supérieure (ENS)/CNRS, 24
6 Rue Lhomond, 75005 Paris, France

7 * Institute for Geophysics and Meteorology, University of Cologne, 50969 Cologne, Germany

8
9
10 This is the Authors Original Manuscript (AOM); that is, the manuscript in its original form; a “preprint”, which has been published
11 in final form at <https://doi.org/10.1002/qj.3292> in the *Quarterly Journal of the Royal Meteorological Society*. Please cite this article as
12 doi: 10.1002/qj.3292.

13
1415

Improved moist-convective rotating shallow water model and its 16 application to instabilities of hurricane-like vortices

17 MASOUD ROSTAMI^{† ‡} and VLADIMIR ZEITLIN^{† *}18 [†] Laboratoire de Météorologie Dynamique/Université Pierre et Marie Curie (UPMC)/Ecole Normale Supérieure (ENS)/CNRS, 24
19 Rue Lhomond, 75005 Paris, France20 [‡] Institute for Geophysics and Meteorology, University of Cologne, 50969 Cologne, Germany

21

22

We show how the two-layer moist-convective rotating shallow water model (mcRSW), which proved to be a simple and robust tool for studying effects of moist convection on large-scale atmospheric motions, can be improved by including, in addition to the water vapour, precipitable water, and the effects of vaporisation, entrainment, and precipitation. Thus improved mcRSW becomes cloud-resolving. It is applied, as an illustration, to model the development of instabilities of tropical cyclone-like vortices.

23 *Key Words:* Moist Convection, Rotating Shallow Water, Tropical Cyclones, Baroclinic Instability

Received ...

24

1. Introduction

25 Massive efforts have been undertaken in recent years in order to improve the quality of weather and climate modelling, and significant
26 progress was achieved. Nevertheless, water vapour condensation and precipitations remain a weak point of weather forecasts, especially
27 long-term ones. Thus, predictions of climate models significantly diverge in what concerns humidity and precipitations (Stevens and
28 Bony 2013). The complexity of thermodynamics of the moist air, which includes phase transitions and microphysics, is prohibitive.
29 That is why the related processes are usually represented through simplified parameterisations in the general circulation models.
30 However, the essentially non-linear, switch character of phase transitions poses specific problems in modelling the water cycle.
31 Parametrisations of numerous physical processes in general circulation models often obscure the role of the water vapour cycle
32 upon the large-scale atmospheric dynamics. The moist-convective rotating shallow water (mcRSW) model was proposed recently,
33 precisely, in order to understand this role in rough but robust terms. The model is based on vertically averaged primitive equations
34 with pseudo-height as vertical coordinate. Instead of proceeding by a direct averaging of the complete system of equations with full
35 thermodynamics and microphysics, which necessitates a series of specific *ad hoc* hypotheses, a hybrid approach is used, consisting in
36 combination of vertical averaging between pairs of isobaric surfaces and Lagrangian conservation of the moist enthalpy (Bouchut et al.
37 2009; Lambaerts et al. 2011). Technically, convective fluxes, i.e. an extra vertical velocity across the material surfaces delimiting the
38 shallow-water layers, are added to the standard RSW model, and are linked to condensation. For the latter a relaxation parametrisation
39 in terms of the bulk moisture of the layer, of the type applied in general circulation models, is used. Thus obtained mcRSW model
40 combines simplicity and fidelity of reproduction of the moist phenomena at large scales, and allows to use efficient numerical tools
41 available for rotating shallow water equations. They also proved to be useful in understanding moist instabilities of atmospheric jets
42 and vortices (Lambaerts et al. 2012; Lahaye and Zeitlin 2016; Rostami and Zeitlin 2017; Rostami et al. 2017).43 The mcRSW model, however, gives only the crudest representation of the moist convection. The water vapour can condense, but
44 after that the liquid water is dropped off, so there are no co-existing phases and no inverse vaporisation phase transition in the model.
45 Yet, it is rather simple to introduce precipitable water in the model, and link it to the water vapour through bulk condensation and
46 vaporisation. At the same time, the convective fluxes present in mcRSW can be associated with entrainment of precipitable water, and
47 its exchanges between the layers, adding more realism in representing the moist convection. Below, we will make these additions to the
48 mcRSW model, and thus obtain an “improved” mcRSW, which we call imcRSW. We will illustrate the capabilities of the new model
49 on the example of moist instabilities of hurricane-like vortices. Multi-layer modelling of tropical cyclones goes back to the pioneering
50 paper Ooyama (1969), which had, however, a limited range due to the constraint of axisymmetry. Strictly barotropic models were
51 also used, e.g. Guinn and Schubert (1993), as well as shallow water models with *ad hoc* parametrisations of latent heat release, e.g.
52 Hendricks et al. (2014). The imcRSW model is a logical development of such approach.

*Corresponding author. Email: zeitlin@lmd.ens.fr

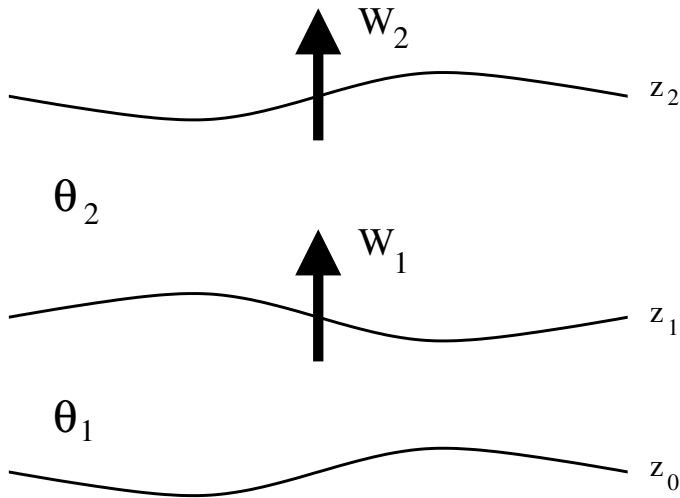


Figure 1. Notations for the simplified two-layer scheme with mass flux across material surfaces. From Lambaerts et al. (2011), with permission of AIP.

53 2. Derivation of the improved mcRSW

54 2.1. Reminder on mcRSW and its derivation

55 Let us recall the main ideas and the key points of derivation of the 2-layer mcRSW model. The starting point is the system of “dry”
 56 primitive equations with pseudo-height as vertical coordinate (Hoskins and Bretherton 1972). We recall that pseudo-height is the
 57 geopotential height for an atmosphere with an adiabatic lapse rate: $z = z_0 (1 - (p/p_0)^{R/c_p})$, where $z_0 = c_p \theta_0 / g$, and the subscript
 58 0 indicates reference sea-level values. Horizontal momentum and continuity equations are vertically averaged between two pairs of
 59 material surfaces z_0, z_1 , and z_1, z_2 , where z_0 is at the ground, and z_2 is at the top. The pseudo-height z being directly related to
 60 pressure, the lower boundary is a “free surface” and the upper boundary is considered to be at a fixed pressure (“rigid lid”). The mean-
 61 field approximation is then applied, consisting, technically, in replacing averages of the products of dynamical variables by products of
 62 averages, which expresses the hypothesis of columnar motion. In the derivation of the “ordinary” RSW the fact that material surfaces
 63 z_i , $i = 0, 1, 2$ are moving, by definition, with corresponding local vertical velocities w_i allows to eliminate these latter. The main
 64 assumption of the mcRSW model is that there exist additional convective fluxes across z_i , such that

$$w_0 = \frac{dz_0}{dt}, \quad w_1 = \frac{dz_1}{dt} + \mathcal{W}_1, \quad w_2 = \frac{dz_2}{dt} + \mathcal{W}_2, \quad (1)$$

65 where $\mathcal{W}_{1,2}$ are contributions from the extra fluxes, whatever their origin, cf. Figure 1. The resulting continuity equations for the
 66 thicknesses of the layers $h_2 = z_2 - z_1$, $h_1 = z_1 - z_0$ are modified in a physically transparent way, acquiring additional source and
 67 sink terms:

$$\begin{aligned} \partial_t h_1 + \nabla \cdot (h_1 \mathbf{v}_1) &= -\mathcal{W}_1, \\ \partial_t h_2 + \nabla \cdot (h_2 \mathbf{v}_2) &= +\mathcal{W}_1 - \mathcal{W}_2. \end{aligned} \quad (2)$$

68 The modified momentum equations contain the terms of the form $\mathcal{W}_i \mathbf{v}$ at the boundaries z_i of the layers. An additional assumption
 69 is, hence, necessary, in order to fix the value of the horizontal velocity at the interface. In the layered models the overall horizontal
 70 velocity, by construction, has the form $\mathbf{v}(z) = \sum_{i=1}^N \mathbf{v}_i H(z_i - z) H(z - z_{i-1})$, where $H(z)$ is Heaviside (step-) function. Assigning a
 71 value to velocity at z_i means assigning a value to the Heaviside function at zero, where it is not defined. This a well-known modelling
 72 problem, and any value between zero and one can be chosen, depending on the physics of the underlying system. In the present
 73 case this choice would reflect the processes in an intermediate buffer layer interpolating between the main layers, and replacing the
 74 sharp interface, if a vertically refined model is used. The “asymmetric” (non-centred) assignment $H(0) = 1$ was adopted in previous
 75 works. The “symmetric” (centred) assignment $H(0) = 1/2$ will be adopted below. This choice does not affect qualitatively the previous
 76 results obtained with mcRSW, however it does affect the forcing terms in conservation laws. It corresponds to a choice of efficiency of
 77 momentum transport between the layers. In this way, the vertically averaged momentum equations become:

$$\begin{cases} \partial_t \mathbf{v}_1 + (\mathbf{v}_1 \cdot \nabla) \mathbf{v}_1 + f \mathbf{k} \times \mathbf{v}_1 = -\nabla \phi(z_1) + g \frac{\theta_1}{\theta_0} \nabla z_1 + \frac{\mathbf{v}_1 - \mathbf{v}_2}{2h_1} \mathcal{W}_1, \\ \partial_t \mathbf{v}_2 + (\mathbf{v}_2 \cdot \nabla) \mathbf{v}_2 + f \mathbf{k} \times \mathbf{v}_2 = -\nabla \phi(z_2) + g \frac{\theta_2}{\theta_0} \nabla z_2 + \frac{\mathbf{v}_2 - \mathbf{v}_1}{2h_2} \mathcal{W}_1 + \frac{\mathbf{v}_1}{2h_2} \mathcal{W}_2, \end{cases} \quad (3)$$

78 Note that, whatever the assignment for Heaviside function, the total momentum of the two-layer system $(z_1 - z_0) \mathbf{v}_1 + (z_2 - z_1) \mathbf{v}_2$ is
 79 locally conserved (modulo the Coriolis force terms). In what follows, will be assuming that $W_2 = 0$.

80 The system is closed with the help of hydrostatic relations between geopotential and potential temperature, which are used to express
 81 the geopotential at the upper levels in terms of the lower-level one:

$$\phi(z) = \begin{cases} \phi(z_0) + g \frac{\theta_1}{\theta_0} (z - z_0) & \text{if } z_0 \leq z \leq z_1, \\ \phi(z_0) + g \frac{\theta_1}{\theta_0} (z_1 - z_0) + g \frac{\theta_2}{\theta_0} (z - z_1) & \text{if } z_1 \leq z \leq z_2, \end{cases} \quad (4)$$

82 The vertically integrated (bulk) humidity in each layer $Q_i = \int_{z_{i-1}}^{z_i} q dz$, $i = 1, 2$, where $q(x, y, z, t)$ is specific humidity, measures
 83 the total water vapour content of the air column, which is locally conserved in the absence of phase transitions. Condensation introduces

84 a humidity sink:

$$\partial_t Q_i + \nabla \cdot (Q_i \mathbf{v}_i) = -C_i, \quad i = 1, 2. \quad (5)$$

85 In the regions of condensation ($C_i > 0$) specific moisture is saturated $q(z_i) = q^s(z_i)$ and the potential temperature $\theta(z_i) + (L/c_p)q^s(z_i)$
86 of an elementary air mass $W_i dt dx dy$, which is rising due to the latent heat release, is equal to the potential temperature of the upper
87 layer θ_{i+1} :

$$\theta_{i+1} = \theta(z_i) + \frac{L}{c_p}q(z_i) \approx \theta_i + \frac{L}{c_p}q(z_i), \quad (6)$$

88 If the background stratification, at constant $\theta(z_i)$ and constant $q(z_i)$, is stable $\theta_{i+1} > \theta_i$, by integrating the three-dimensional equation
89 of moist-adiabatic processes

$$\frac{d}{dt} \left(\theta + \frac{L}{c_p}q \right) = 0. \quad (7)$$

90 we get

$$\mathcal{W}_i = \beta_i C_i, \quad \beta_i = \frac{L}{c_p(\theta_{i+1} - \theta_i)} \approx \frac{1}{q(z_i)} > 0. \quad (8)$$

91 In this way the extra vertical fluxes in (3), (2) are linked to condensation. For the system to be closed, condensation should be connected
92 to moisture. This is done via the relaxation parametrisation, where the moisture relaxes with a characteristic time τ_c towards the
93 saturation value Q^s , if this threshold is crossed:

$$C_i = \frac{Q_i - Q_i^s}{\tau_c} H(Q_i - Q_i^s). \quad (9)$$

94 Essentially nonlinear, switch character of the condensation process is reflected in this parameterisation, which poses no problem in
95 finite-volume numerical scheme we are using below. For alternative, e.g. finite-difference schemes smoothing of the Heaviside function
96 could be used. In what follows we consider the two-layer model assuming that the upper layer is dry, and even with entrainment of
97 water from the lower moist layer, water vapour in this layer is far from saturation, so the convective flux W_2 is negligible. In this way
98 we get the mcRSW equations for such configuration:

$$\begin{cases} \partial_t \mathbf{v}_1 + (\mathbf{v}_1 \cdot \nabla) \mathbf{v}_1 + f \mathbf{k} \times \mathbf{v}_1 = -g \nabla(h_1 + h_2) + \frac{\mathbf{v}_1 - \mathbf{v}_2}{2h_1} \beta C, \\ \partial_t \mathbf{v}_2 + (\mathbf{v}_2 \cdot \nabla) \mathbf{v}_2 + f \mathbf{k} \times \mathbf{v}_2 = -g \nabla(h_1 + sh_2) + \frac{\mathbf{v}_1 - \mathbf{v}_2}{2h_2} \beta C, \\ \partial_t h_1 + \nabla \cdot (\mathbf{h}_1 \mathbf{v}_1) = -\beta C, \\ \partial_t h_2 + \nabla \cdot (\mathbf{h}_2 \mathbf{v}_2) = +\beta C, \\ \partial_t Q + \nabla \cdot (Q \mathbf{v}_1) = -C, \quad C = \frac{Q - Q^s}{\tau_c} H(Q - Q^s) \end{cases}, \quad (10)$$

99 where $s = \theta_2/\theta_1 > 1$ is the stratification parameter, $\mathbf{v}_1 = (u_1, v_1)$ and $\mathbf{v}_2 = (u_2, v_2)$ are the horizontal velocity fields in the lower and
100 upper layer (counted from the bottom), with u_i zonal and v_i meridional components, and h_1, h_2 are the thicknesses of the layers, and
101 we will be considering the Coriolis parameter f to be constant.

102 As in the previous studies with mcRSW, we will not develop sophisticated parameterisations of the boundary layer and of fluxes
103 across the lower boundary of the model. Such parameterisations exist in the literature (Schecter and Dunkerton 2009), and may be
104 borrowed, if necessary. We will limit ourselves by the simplest version of the exchanges with the boundary layer, with a a source of
105 bulk moisture in the lower layer due to surface evaporation E . The moisture budget thus becomes:

$$\partial_t Q + \nabla \cdot (Q \mathbf{v}_1) = E - C \quad (11)$$

106 The simplest parametrisations being used in the literature are the relaxational one

$$E = \frac{\hat{Q} - Q}{\tau_E} H(\hat{Q} - Q), \quad (12)$$

107 and the one where surface evaporation is proportional to the wind, which is plausible for the atmosphere over the oceanic surface:

$$E \propto |\mathbf{v}|; \quad (13)$$

108 The two can be combined, in order to prevent the evaporation due to the wind to continue beyond the saturation:

$$E_s = \frac{\hat{Q} - Q}{\tau_E} |\mathbf{v}| H(\hat{Q} - Q). \quad (14)$$

109 The typical evaporation relaxation time τ_E is about one day in the atmosphere, to be compared with τ_c , which is about an hour. Thus
110 $\tau_E \gg \tau_c$. \hat{Q} can be taken equal, or close to Q_s , as we are doing, but not necessarily, as it represents complex processes in the boundary
111 layer, and can be, in turn, parametrised.

112 2.2. Improving the mcRSW model

113 An obvious shortcoming of the mcRSW model presented above is that, although it includes condensation and related convective fluxes,
 114 the condensed water vapour disappears from the model. In this sense, condensation is equivalent to precipitation in the model. Yet, as is
 115 well-known, condensed water remains in the atmosphere in the form of clouds, and precipitation is switched only when water droplets
 116 reach a critical size. It is easy to include precipitable water in the model in the form of another advected quantity with a source due
 117 to condensation, and a sink due to vaporisation, the latter process having been neglected in the simplest version of mcRSW. We thus
 118 introduce a bulk amount of precipitable water, $W(x, y, t)$, in the air column of a given layer. It obeys the following equation in each
 119 layer:

$$\partial_t W + \nabla \cdot (W \mathbf{v}) = +C - V, \quad (15)$$

120 where V denotes vaporisation. Vaporisation can be parametrised similarly to condensation:

$$P = \frac{Q_s - Q}{\tau_v} H(Q_s - Q). \quad (16)$$

121 Opposite to the condensation, vaporisation engenders cooling, and hence a downward convective flux, which can be related to the
 122 background stratification along the same lines as upward flux due to condensation:

$$\mathcal{W}_v = -\beta^* V, \quad \beta^* = \frac{L^*}{C_v(\theta_2 - \theta_1)}, \quad (17)$$

123 where L^* is the latent heat absorption coefficient, C_v is specific heat of vaporisation. β^* is an order of magnitude smaller than β . There
 124 is still no precipitation sink in (15). Such sink can be introduced, again as a relaxation with a relaxation time τ_p , and conditioned by
 125 some critical bulk amount of precipitable water in the column:

$$P = \frac{W - W_{cr}}{\tau_p} H(W - W_{cr}). \quad (18)$$

126 The extra fluxes (17) due to cooling give rise to extra terms in mass and momentum equations of the model in each layer. Another
 127 important phenomenon, which is absent in the simplest version of mcRSW is the entrainment of liquid water by updrafts. This process
 128 can be modelled in a simple way as a sink in the lower-layer precipitable water equation, which is proportional, with some coefficient
 129 γ , to the updraft flux, and hence, to condensation, and provides a corresponding source of precipitable water in the upper-layer.

130 Including the above-described modifications in the mcRSW models, and neglecting for simplicity 1) condensation and precipitations
 131 in the upper layer, by supposing that it remains far from saturation, 2) vaporisation in the lower layer, which is supposed to be close to
 132 saturation, we get the following system of equations:

$$\left\{ \begin{array}{l} \frac{d_1 \mathbf{v}_1}{dt} + f \hat{z} \times \mathbf{v}_1 = -g \nabla (h_1 + h_2) + \left(\frac{\beta C - \beta^* V}{h_1} \right) \left(\frac{\mathbf{v}_1 - \mathbf{v}_2}{2} \right), \\ \frac{d_2 \mathbf{v}_2}{dt} + f \hat{z} \times \mathbf{v}_2 = -g \nabla (h_1 + sh_2) + \left(\frac{\beta C - \beta^* V}{h_2} \right) \left(\frac{\mathbf{v}_1 - \mathbf{v}_2}{2} \right), \\ \partial_t h_1 + \nabla \cdot (h_1 \mathbf{v}_1) = -\beta C + \beta^* V, \\ \partial_t h_2 + \nabla \cdot (h_2 \mathbf{v}_2) = +\beta C - \beta^* V, \\ \partial_t W_1 + \nabla \cdot (W_1 \mathbf{v}_1) = +(1 - \gamma) C - P, \\ \partial_t W_2 + \nabla \cdot (W_2 \mathbf{v}_2) = +\gamma C - V, \\ \partial_t Q_1 + \nabla \cdot (Q_1 \mathbf{v}_1) = -C + E, \\ \partial_t Q_2 + \nabla \cdot (Q_2 \mathbf{v}_2) = V, \end{array} \right. \quad (19)$$

133 where $d_i \dots / dt = \partial_t \dots + (\mathbf{v}_i \cdot \nabla) \dots$, $i = 1, 2$. Here C is condensation in the lower layer considered to be close to saturation, W_i is
 134 the bulk amount of precipitable water and Q_i bulk humidity in each layer, γ is the entrainment coefficient, V is vaporisation in the
 135 upper layer, considered as mostly dry. C , V , and P obey (9), (16), (18), respectively. Note that if the above-formulated hypotheses of
 136 mostly dry upper layer, and almost saturated lower layer are relaxed (or get inconsistent during simulations), the missing condensation,
 137 precipitation, and vaporisation in the corresponding layers can be easily restituted according to the same rules.

138 2.3. Conservation laws in the improved mcRSW model

139 As was already said, the total momentum of the system is locally conserved in the absence of the Coriolis force ($f \rightarrow 0$), as can be seen
 140 by adding the equations for the momentum density in the layers:

$$\begin{aligned} (\partial_t + \mathbf{v}_1 \cdot \nabla) (h_1 \mathbf{v}_1) + h_1 \mathbf{v}_1 \nabla \cdot \mathbf{v}_1 + f \hat{z} \times (h_1 \mathbf{v}_1) = \\ -g \nabla \frac{h_1^2}{2} - gh_1 \nabla h_2 - \left(\frac{\mathbf{v}_1 + \mathbf{v}_2}{2} \right) (\beta C - \beta^* V) \end{aligned} \quad (20a)$$

$$\begin{aligned} (\partial_t + \mathbf{v}_2 \cdot \nabla) (h_2 \mathbf{v}_2) + h_2 \mathbf{v}_2 \nabla \cdot \mathbf{v}_2 + f \hat{z} \times (h_2 \mathbf{v}_2) = \\ -gs \nabla \frac{h_2^2}{2} - gh_2 \nabla h_1 + \left(\frac{\mathbf{v}_1 + \mathbf{v}_2}{2} \right) (\beta C - \beta^* V) \end{aligned} \quad (20b)$$

142 The last term in each equation corresponds to a Rayleigh drag produced by vertical momentum exchanges due to convective fluxes.

143 The total mass (thickness) $h = h_1 + h_2$ is also conserved, while the mass in each layer $h_{1,2}$ is not. However, we can construct a
 144 moist enthalpy in the lower layer

$$m_1 = h_1 - \beta Q_1 - \beta^* W_2, \quad (21)$$

145 which is locally conserved, if entrainment and surface evaporation are absent:

$$\partial_t m_i + \nabla \cdot (m_i \mathbf{v}_i) = 0, \quad i = 1, 2. \quad (22)$$

146 The inclusion of precipitable water in the upper layer in (21) is necessary to compensate the downward mass flux due to vaporisation.

147 The dry energy of the system $E = \int dx dy (e_1 + e_2)$ is conserved in the absence of diabatic effects, where the energy densities of the
148 layers are:

$$\begin{cases} e_1 = h_1 \frac{\mathbf{v}_1^2}{2} + g \frac{h_1^2}{2}, \\ e_2 = h_2 \frac{\mathbf{v}_2^2}{2} + gh_1 h_2 + sg \frac{h_2^2}{2}. \end{cases}$$

149 In the presence of condensation and vaporisation, the energy budget changes and the total energy density $e = e_1 + e_2$ is not locally
150 conserved, acquiring a sink/source term:

$$\partial_t e = -\nabla \cdot \mathbf{f}_e - (\beta C - \beta^* V)g(1-s)h_2, \quad (23)$$

151 where \mathbf{f}_e is the standard energy density flux in the two-layer model. For the total energy $E = \int dx dy e$ of the closed system we thus get
152

$$\partial_t E = (\beta C - \beta^* V)g(s-1) \int dx dy h_2. \quad (24)$$

153 For stable stratifications $s > 1$, the r.h.s. of this equation represents an increase (decrease) of potential energy due to upward (downward)
154 convective fluxes due to condensation heating (vaporisation cooling). Note that with “asymmetric” assignment of Heaviside function
155 at zero, an extra term corresponding to kinetic energy loss due to Rayleigh drag would appear in the energy budget, cf [Lambaerts et al. \(2011\)](#).
156

Potential vorticity (PV) is an important characteristics of the flow. In the presence of diabatic effects it ceases to be a Lagrangian invariant, and evolves in each layer as follows:

$$\frac{d_1}{dt} \left(\frac{\zeta_1 + f}{h_1} \right) = \left(\frac{\zeta_1 + f}{h_1} \right) \cdot \frac{(\beta C - \beta^* V)}{h_1} + \frac{\hat{\mathbf{z}}}{h_1} \cdot \left[\nabla \times \left(\frac{\mathbf{v}_1 - \mathbf{v}_2}{2} \cdot \frac{\beta C - \beta^* V}{h_1} \right) \right], \quad (25a)$$

$$\frac{d_2}{dt} \left(\frac{\zeta_2 + f}{h_2} \right) = - \left(\frac{\zeta_2 + f}{h_2} \right) \cdot \frac{(\beta C - \beta^* V)}{h_2} + \frac{\hat{\mathbf{z}}}{h_2} \cdot \left[\nabla \times \left(\frac{\mathbf{v}_1 - \mathbf{v}_2}{2} \cdot \frac{\beta C - \beta^* V}{h_2} \right) \right], \quad (25b)$$

157 where $\zeta_i = \hat{\mathbf{z}} \cdot (\nabla \times \mathbf{v}_i) = \partial_x v_i - \partial_y u_i$ ($i = 1, 2$) is relative vorticity, and $q_i = (\zeta_i + f)/h_i$ is potential vorticity in each layer. One can
158 construct a moist counterpart of potential vorticity in the lower layer with the help of the moist enthalpy (21), cf [Lambaerts et al. \(2011\)](#):
159

$$q_{1m} = \frac{\zeta_1 + f}{m_1}. \quad (26)$$

160 The moist PV is conserved in the lower layer, modulo the Rayleigh drag effects:

$$\frac{d_1}{dt} \left(\frac{\zeta_1 + f}{m_1} \right) = +\hat{\mathbf{z}} \cdot \left[\nabla \times \left(\frac{\mathbf{v}_1 - \mathbf{v}_2}{2} \cdot \frac{\beta C - \beta^* V}{m_1^2} \right) \right]. \quad (27)$$

161 Note that the “asymmetric” assignment of the value of the step-function, which was discussed above, renders the moist PV in the lower
162 layer conserved.

163 3. Illustration: application of improved mcRSW model to moist instabilities of hurricane-like 164 vortices

165 3.1. Motivations

166 We will illustrate the capabilities of the improved mcRSW, the imcRSW, on the example of moist instabilities of hurricane-like vortices.
167 The mcRSW model, in its simplest one-layer version, captures well the salient properties of moist instabilities of such vortices, and
168 clearly displays an important role of moisture in their development ([Lahaye and Zeitlin 2016](#)). Below we extend the analysis of [Lahaye and Zeitlin \(2016\)](#) to baroclinic tropical cyclones (TC), and use the imcRSW to check the role of new phenomena included in the
169 model. Some questions which remained unanswered will be addressed, as well as new ones, possible to answer with the improved
170 version of the model. In particular, we will investigate the influence of the size of TC (the radius of maximum wind) upon the structure
171 of the most unstable mode, the role of vertical shear, and the evolution of inner and outer cloud bands at nonlinear stage of instability.
172

173 3.2. Fitting velocity and vorticity distribution of the hurricanes

174 We begin with building velocity and vorticity profiles of a typical TC within the two-layer model. An analytic form of the velocity
175 profile is convenient both for the linear stability analysis, and for initialisations of the numerical simulations, so we construct a simple
176 analytic fit with a minimal number of parameters. It has the form which is consistent with [Mallen et al. \(2005\)](#) where flight-level

Table 1. Parameters of the background vortices. BCW(S): weak(strong) baroclinic, BTW: weak “barotropic”, without vertical shear, l : the most unstable azimuthal mode

config.	l	ϵ_1	ϵ_2	α_1	α_2	β_1	β_2	m_1	m_2	r_{01}	r_{02}
BCS	3	0.41	0.49	4.5	4.5	0.180	0.178	48	47.5	0.01	0.0101
BTW	4	0.4	0.40	2.25	2.25	0.25	0.25	14	14	0.1	0.1
BCW	4	0.4	0.36	2.25	2.25	0.25	0.237	14	12.6	0.1	0.115

177 observations were collected from Atlantic and eastern Pacific storms during 1977 – 2001:

$$V_i(r) = \begin{cases} \epsilon_i \frac{[(r - r_0)^{\alpha_i} e^{-m_i(r - r_0)^{\beta_i}}]}{\max[(r - r_0)^{\alpha_i} e^{-m_i(r - r_0)^{\beta_i}}]}, & r \geq r_0, \\ m_0 r, & r \leq r_0. \end{cases} \quad (28)$$

Here $i = 1, 2$ indicate the lower and upper layer, respectively, r is the non-dimensional distance from the center, ϵ_i measures the intensity of the velocity field, r_0 sets the non-dimensional distance of maximum wind from the centre, and other parameters allow to fit the shape of the distribution. A cubic Hermite interpolation across $r = r_0$ is made to prevent discontinuity in vorticity. Here and below we use a simple scaling where the distances are measured in units of barotropic deformation radius $R_d = \sqrt{gH}/f$, and velocities are measured in units of \sqrt{gH} , where H is the total thickness of the atmospheric column at rest. (Hence, the parameter ϵ acquires a meaning of Froude number). Under this scaling the Rossby number of the vortex is proportional to the inverse of the non-dimensional radius of maximum wind (RMW). A useful property of this parametrisation is a possibility to tune the ascending or descending trends of the wind near and far from the velocity peak. Velocity is normalised in a way that the maximum velocity is equal to ϵ . We suppose that velocity profile (28) corresponds to a stationary solution of “dry” equations of the model. Such solutions obey the cyclo-geostrophic balance in each layer:

$$\left(\frac{V_1}{r} + f \right) V_1 = g \frac{\partial}{\partial r} (H_1 + H_2), \quad (29a)$$

$$\left(\frac{V_2}{r} + f \right) V_2 = g \frac{\partial}{\partial r} (H_1 + \alpha H_2), \quad (29b)$$

178 so the related $H_i(r)$ are obtained by integrating these equations using (28). The radial distribution of the relative vorticity in the vortex
179 is given by $(1/r)d[rV(r)]/dr$. It should be emphasised that the radial gradient of the PV corresponding to the profile (28) has sign
180 reversal, and hence the instability of the vortex is expected. Typical velocity and vorticity fields of an intense (category 3) vortex are
presented in Figure 2.

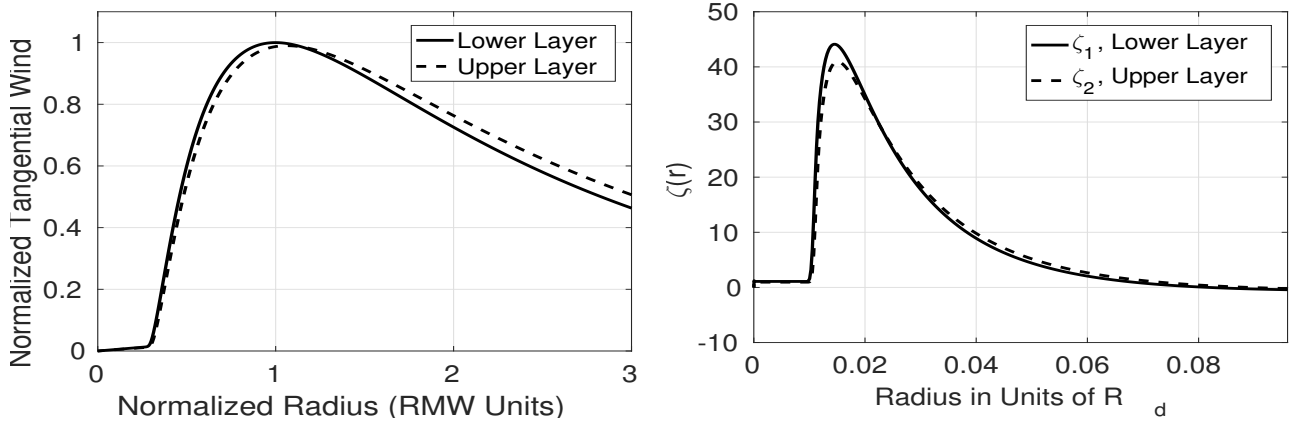


Figure 2. Normalised radial structure of azimuthal tangential wind with a fixed slope close to the centre (left panel) and relative vorticity (right panel) in both layers corresponding to the BCS vortex in Table 1.

181 In what follows, we will be studying instabilities of thus constructed vortices, and their nonlinear saturation. The strategy will be
182 the same as in (Lahaye and Zeitlin 2016): namely, we identify the unstable modes of the vortex by performing detailed linear stability
183 analysis of the “dry” adiabatic system, with switched-off condensation and vaporisation, and then use the unstable modes to initialise
184 numerical simulations of nonlinear saturation of the instability, by superimposing them, with small amplitude, onto the background
185 vortex. We will give below the results of numerical simulations of developing instabilities for three typical configurations which are
186 presented in Table 1: weak barotropic (BTW) and baroclinic (BCW), and strong baroclinic (BCS) vortices.

188 3.3. Results of the linear stability analysis: the most unstable mode and its dependence on the radius of maximal wind

189 By applying the standard linearisation procedure and considering small perturbations to the axisymmetric background flow, we
190 determine eigenfrequencies and eigenmodes of the “dry” system linearised about the background vortex. The technicalities of such

191 analysis are the same as in Lahaye and Zeitlin (2015) extended to the two-layer configuration as in Rostami and Zeitlin (2017), and we
 192 pass directly to the results, which we will not give in detail either, limiting ourselves by what is necessary for numerical simulations in
 193 the next section.

The most unstable mode with azimuthal wavenumber $l = 3$ of the BCS vortex is presented in Fig. 3. The unstable mode of Figure 3

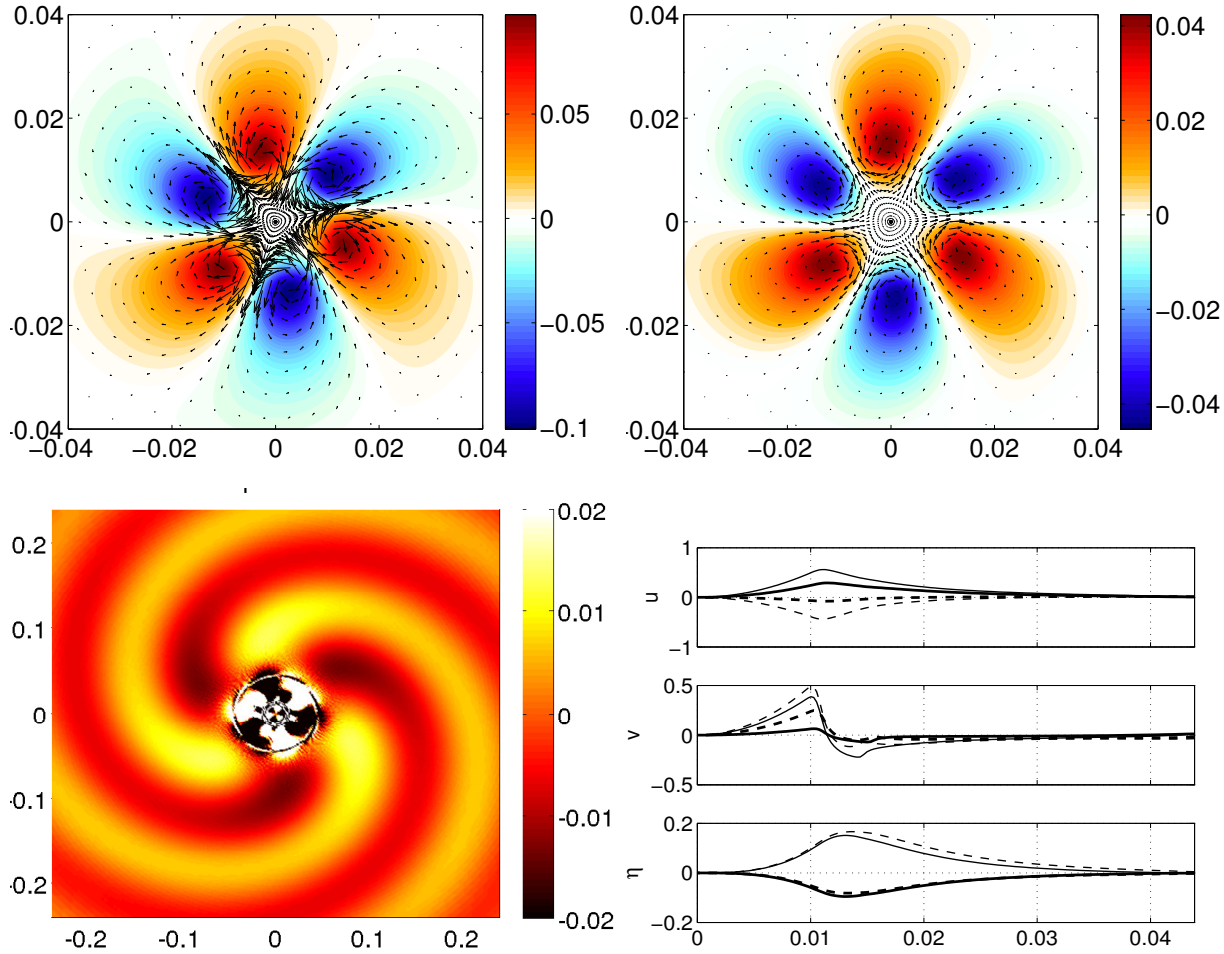


Figure 3. *Upper row:* Pressure and velocity fields in the $x - y$ plane in the lower (left panel) and upper (right panel) layers corresponding to the most unstable mode with azimuthal wavenumber $l = 3$ of the BCS vortex of Table 1. *Lower row:* left panel- corresponding divergence field of the most unstable mode, right panel - radial structure of three components of the most unstable mode: pressure anomaly η , and radial (v) and tangential (u) components of velocity ; dashed (solid) lines: imaginary (real) part, thick (thin) lines correspond to upper (lower) layer. Note that the domain in the lower left panel is \approx ten times larger than that of the upper panels.

194 is clearly of mixed Rossby - inertia gravity wave type. Such unstable modes of hurricane-like vortices are well documented in literature,
 195 both in shallow-water models (Zhong and Zhang 2014) and full 3D models (Menelau et al. 2016). It should be stressed that at Rossby
 196 numbers which are about 40 and small Burger number, as can be inferred from the right panel of Fig. 2, the vortex Rossby wave part of
 197 the unstable mode, which is known since the work (Montgomery and Kallenbach 1997) and is clearly seen in the upper panels of Fig.
 198 3, is inevitably coupled to inertia-gravity wave field through Lighthill radiation mechanism, cf. Zeitlin (2008).

199 The most unstable modes of BCW and BTW vortices have wavenumber $l = 4$. With our scaling the strength of the vortex is inversely
 200 proportional to its non-dimensional RMW , and thus the structure of the most unstable mode depends on RMW . Yet, as follows from
 201 Figure 4, the mode $l = 4$ is dominant through the wide range of RMW . In general, higher values of RMW correspond to higher
 202 azimuthal wavenumbers and lower growth rates.

204 3.4. Nonlinear evolution of the instability

205 We now use the unstable modes identified by the linear stability analysis to initialise numerical simulation of nonlinear evolution of the
 206 instability. We superimpose the unstable modes with weak amplitude (several per cent with respect to the background values) onto the
 207 vortex and trace the evolution of the system, as follows from numerical simulations with finite-volume well-balanced scheme developed
 208 for moist-convective RSW model (Bouchut et al. 2009). Numerical simulations with each of the vortex configurations of Table 1 were
 209 performed both in “dry” (M), with diabatic effects switched off, and moist-convective (MCEV) environments.

210 The values of parameters controlling condensation, evaporation, vaporisation, and precipitation in MCEV environment are given in
 211 Table 2. It must be stressed that amount of precipitable water in each layer is highly sensitive to the values of parameters, especially to
 212 the intensity of surface evaporation. Condensation and precipitation time scales are chosen to be short, just few time steps Δt , while
 213 vaporisation and surface evaporation time-scales are much larger which is consistent with physical reality. Changing these parameters
 214 within the same order of magnitude does not lead to qualitative changes in the results. W_{cr} is an adjustable parameter that controls
 215 precipitation and γ controls entrainment of condensed water. The MCEV simulations were initialised with spatially uniform moisture

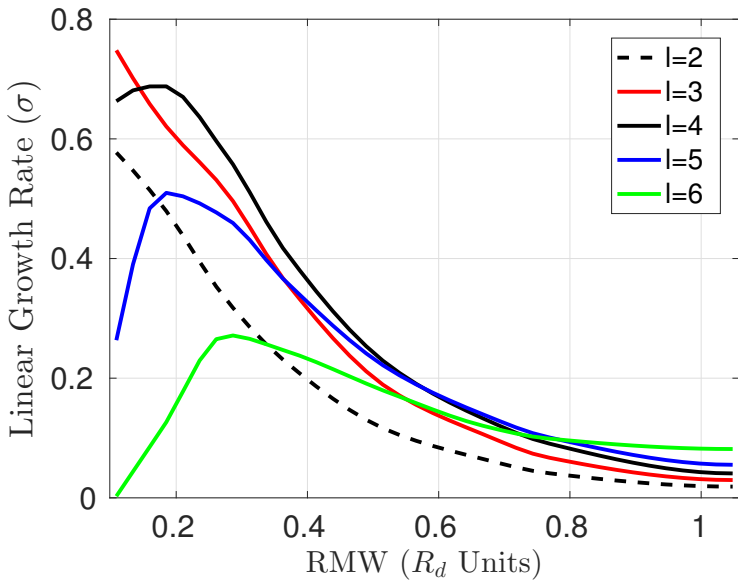


Figure 4. Dependence of the linear growth rates (in units of f^{-1}) of the unstable modes with different azimuthal wavenumbers on the radius of maximum wind (RMW).

Table 2. The values of parameters controlling condensation: τ_c , Q^s , stratification: $s = \theta_2/\theta_1$, evaporation: τ_E , vaporisation: τ_v , and precipitation: W_{cr} , τ_p . Δt is the time-step of the code.

τ_c	Q^s	\hat{Q}	s	τ_E	τ_v	W_{cr}	τ_p	γ
$5\Delta t$	0.75	$\approx Q^s$	1.5	$200\Delta t \approx 1$ day	$10\tau_c$	0.01	$3\Delta t$	0.3

216 content. We present below some outputs of the simulations, illustrating different aspects of moist vs “dry” evolution, and difference in
 217 behaviour of baroclinic and barotropic vortices.

218 3.4.1. Evolution of potential vorticity

219 We start by evolution of the PV field of the weak cyclone, as it is understandably slower than the evolution of the strong one, and
 220 different stages can be clearly distinguished. The evolution of potential vorticity in both layers during nonlinear saturation of the
 221 instability of the BCW vortex in MCEV environment is presented in Fig. 5, 6. The simulations show formation of a transient polygonal
 222 pattern inside the RMW at initial stages, with a symmetry of the most unstable linear mode. The patterns of this kind are frequently
 223 observed (Muramatsu 1986; Lewis and Hawkins 1982; Muramatsu 1986; Kuo et al. 1999). The polygon is further transformed into an
 224 annulus of high PV. Such annuli of elevated vorticity (the so-called *hollow PV towers* (Hendricks and Schubert 2010)) are found in both
 225 moist-convective and dry cases. It is worth mentioning that the growth of the primary unstable mode is accompanied by enhancement
 226 of outer gravity-wave field, as follows from the divergence field presented in Fig. 7.

227 As follows from Figs. 5, 6 the polygon loses its shape at $t \approx 17$. At this time the modes with azimuthal wavenumbers $l = 1, 2$
 228 are being produced by nonlinear interactions, and start to grow and interact with the polygonal eye-wall, which leads to symmetry
 229 loss by the core. A secondary, dipolar instability of the core thus develops, and gives rise to formation of an elliptical central vortex,
 230 corresponding to azimuthal mode $l = 1$, and of a pair of satellite vortices indicating the presence of $l = 2$ mode. The interaction of
 231 initial $l = 4$ mode with emerging $l = 1$ and $l = 2$ modes is accompanied by inertia-gravity wave (IGW) emission, and enhancement
 232 of water vapour condensation that will be discussed below. It should be emphasised that interaction between $l = 2$ mode and elliptical
 233 eye, of the kind we observe in simulations, was described in TC literature, e.g. Kuo et al. (1999), where reflectivity data from a Doppler
 234 radar were used to hypothesise that it was due to azimuthal propagation of $l = 2$ vortex Rossby waves around the eye-wall.

235 Further nonlinear evolution consists in breakdown of the central ellipse with subsequent axisymmetrisation of the PV field, and its
 236 intensification at the center. This process characterises the evolution of both BTW (not shown) and BCW vortices, but is more efficient
 237 in the baroclinic case, as follows from Fig. 8. As seen in the Figure, the azimuthal velocity in the core region with $r < 0.5RMW$
 238 is subject to strong intensification. The exchanges of PV between the eye-wall and the eye, and intensification are known from the
 239 barotropic simulations (Montgomery and Kallenbach 1997; Schubert et al. 1999; Lahaye and Zeitlin 2016). As we see in Fig. 8, the
 240 intensification is enhanced by baroclinicity of the background vortex. This is confirmed by Fig. 9, and by Fig. 10, which illustrate the
 241 enhancement effect of both moist convection and baroclinicity upon palinstrophy, which is defined as

$$\mathcal{P}(t) = \iint \frac{1}{2} \nabla \zeta \cdot \nabla \zeta dx dy, \quad (30)$$

242 in each layer, and which diagnoses the overall intensity of vorticity gradients.

243 It is worth emphasising that, because of higher vorticity and smaller RMW, the axisymmetric steady state is achieved in the lower
 244 layer more rapidly than in the upper one in the case of baroclinic vortices.

245 In the case of intense vortex, nonlinear evolution of the instability follows similar scenario, but is considerably accelerated, as follows
 246 from Fig. 11.

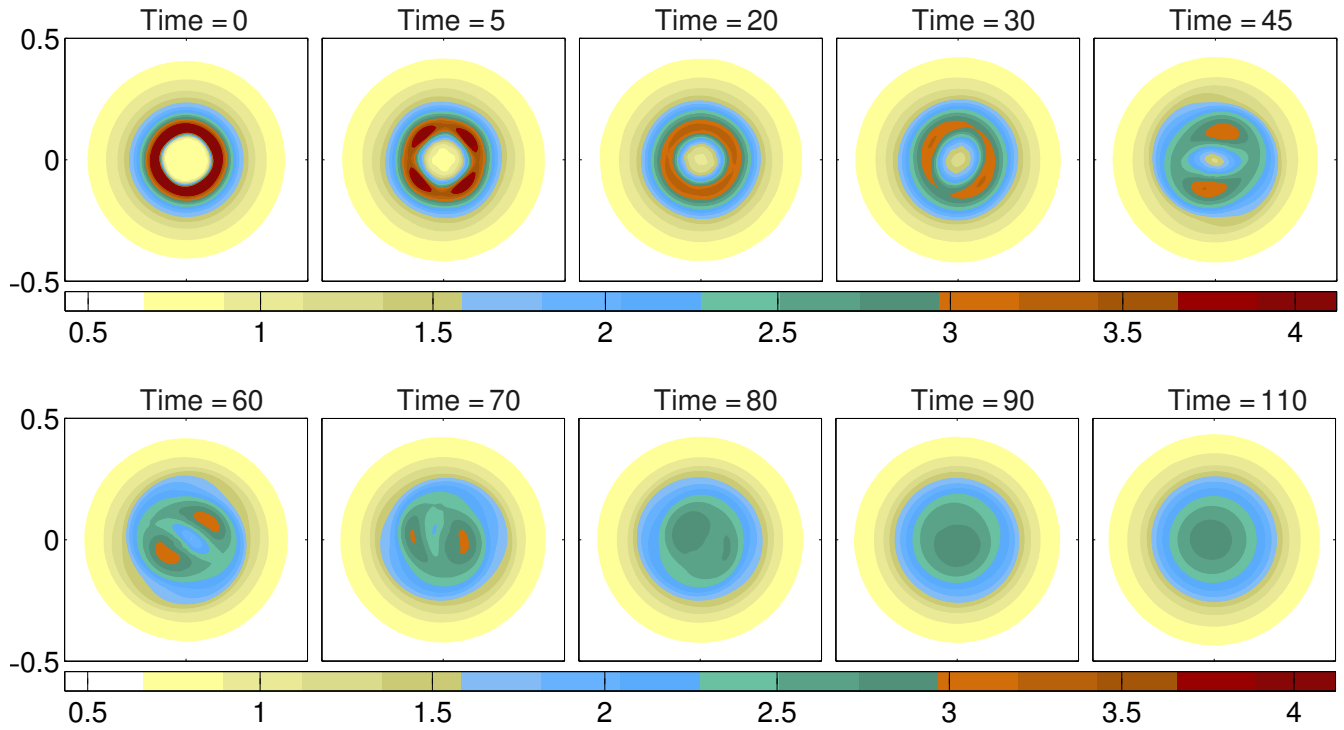


Figure 5. Nonlinear evolution of the most unstable $l = 4$ mode superimposed onto the background BCW vortex in MCEV environment, as seen in potential vorticity field in the lower layer. Formation of meso-vortices (zones of enhanced PV in the vorticity ring) is clearly seen, giving way to axisymmetrisation and monotonisation of the PV profile. Time is measured in units of f^{-1} .

247 3.4.2. Spiral cloud bands

248 Tropical cyclones exhibit specific cloud patterns. The new version of the model gives a possibility to follow clouds and precipitation, and it is interesting to test its capability to produce realistic cloud patterns. There are two types of cloud and rain bands associated with 249 tropical cyclones, as reported in literature: the inner bands, that are situated close to the vortex core, within ≈ 2 RMW, and the outer 250 spiral bands located farther from the centre and having larger horizontal scales (Guinn and Schubert 1993; Wang 2009). Fig. 12 shows 251 formation of inner and outer cloud bands, the latter having characteristic spiral form, during nonlinear evolution of the instability. Spiral 252 cloud bands are related to inertia-gravity “tail” of the developing unstable mode. The link of spiral bands to inertia-gravity waves in 253 “dry” RSW model of hurricanes was discussed in literature (Zhong et al. 2009). Here we see it in “cloud-resolving” imcRSW. It is to 254 be stressed that amount of clouds strongly depends on the initial water vapour content. If it is closer to the saturation value, the amount 255 of clouds and precipitation obviously increases and eventually covers the whole vortex.

257 4. Conclusions and discussion

258 Thus, we have shown that the moist-convective rotating shallow water model “augmented” by adding precipitable water, and 259 relaxational parametrisations of related processes of vaporisation, precipitation, together with entrainment, is capable to capture some 260 salient features of the evolution of instabilities of hurricane-like vortices in moist-convective environment, and allows to analyse the 261 importance of moist processes on the life-cycle of these instabilities. There exist extended literature on the dynamics of the hurricanes 262 eyewall, with tentative explanations in terms of transient internal gravity waves, which form spiral bands, cf. Lewis and Hawkins 263 (1982) Willoughby (1978), Kurihara (1976), or alternative explanations Guinn and Schubert (1993) in terms of PV dynamics and 264 vortex Rossby waves. Thus Schubert et al. (1999) obtained formation of polygonal eyewalls as a result of barotropic instability near the 265 radius of maximum wind in a purely barotropic model, without gravity waves. A detailed analysis of instabilities of tropical cyclones 266 was undertaken with a cloud-resolving model in Naylor and Shecter (2014), and showed that the results of Schubert et al. (1999) gave 267 a useful first approximation for the eyewall instabilities. As was already mentioned in section 3.3, at high Rossby numbers the vortex 268 Rossby wave motions are inevitably coupled to inertia-gravity waves, and our linear stability analysis confirms this fact. The mixed 269 character of the wave perturbations of axisymmetric hurricane-like vortices was abundantly discussed in literature, e.g. Zhong et al. 270 (2009). A detailed analysis of instabilities of hurricane-like vortices in continuously stratified fluid was given recently by Menelau et al. 271 (2016), where it was shown that the inertia-gravity part of the unstable modes intensifies with increasing Froude number. The vortex 272 profiles used above in section 3.2 have moderate Froude numbers, and the corresponding unstable modes have weak inertia-gravity 273 tails. They are, however, sufficient to generate spiral cloud patterns, as we showed. The development of the instability of the eyewall 274 proper at early stages (up to $\approx 40f^{-1}$) is only weakly influenced by moist convection, in accordance with findings of Naylor and 275 Shecter (2014). This can be seen from comparison of the right and left panels of Fig. 9 and from Fig. 10.

276 An advantage of our model, as compared to simple barotropic models, is its ability to capture both vorticity and inertia gravity waves 277 dynamics. Another advantage is that the model includes the moist convection and couples it to dynamics and water vapour transport

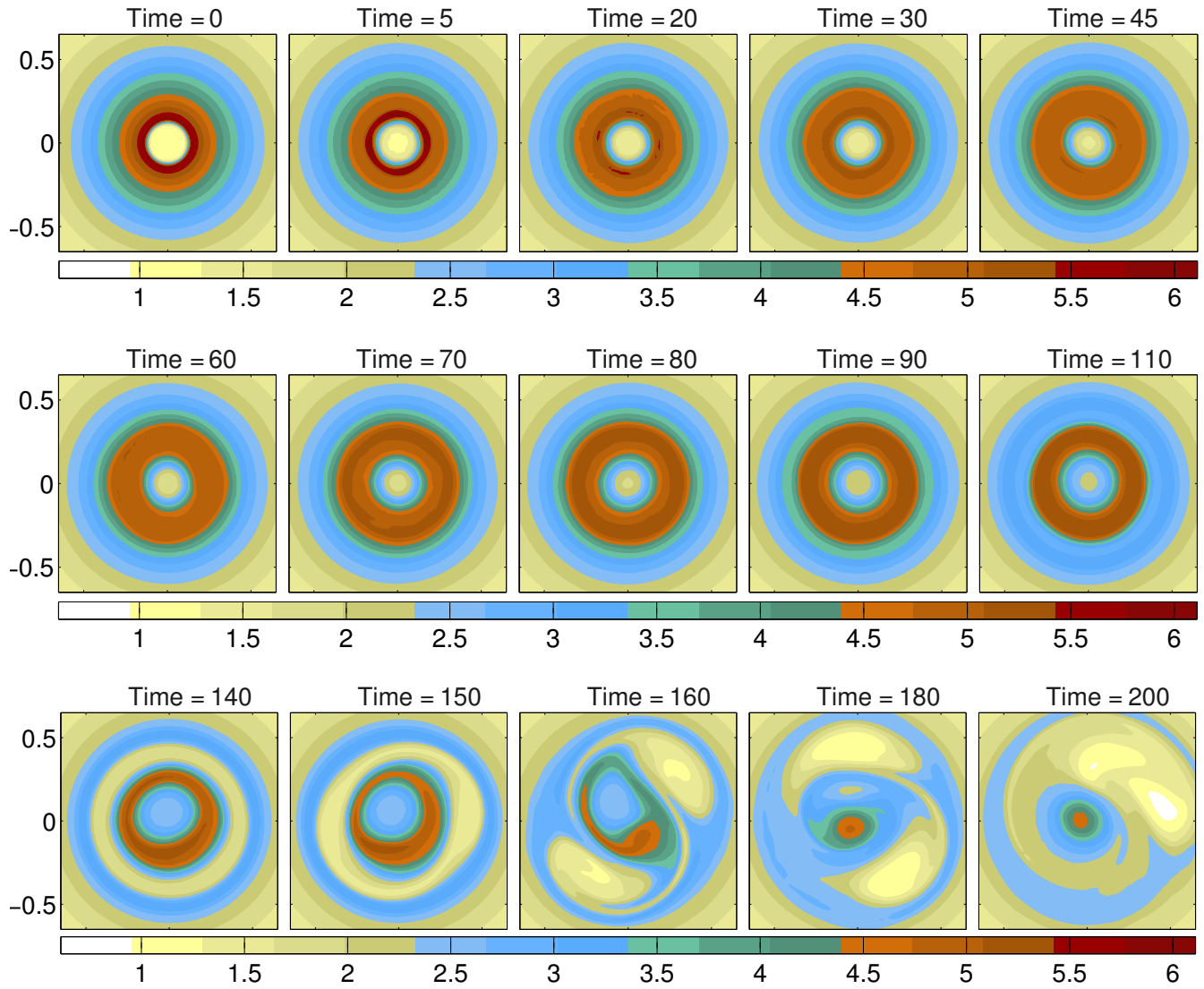


Figure 6. Same as in Fig. 5, but for the upper layer.

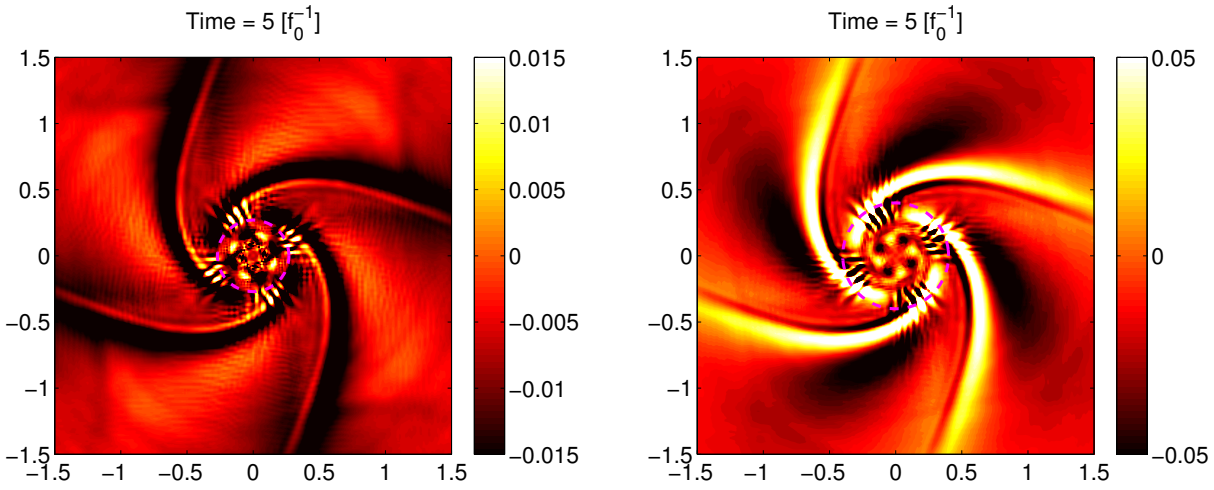


Figure 7. Divergence field at $t = 5[f_0^{-1}]$ in the lower (left panel) and upper (right panel) layers during the evolution of the instability of the BCW vortex in moist-convective and evaporating environment. Dashed line in the right panel represents the radius of maximum wind. Spiral structure, corresponding to inertia gravity wave ‘tail’ of the unstable mode is seen to persist.

278 and condensation in a self-consistent way, as compared e.g. with Hendricks et al. (2014), where the latent heat release due to the moist
279 convection was introduced via *ad hoc* mass sink in rotating shallow water model.

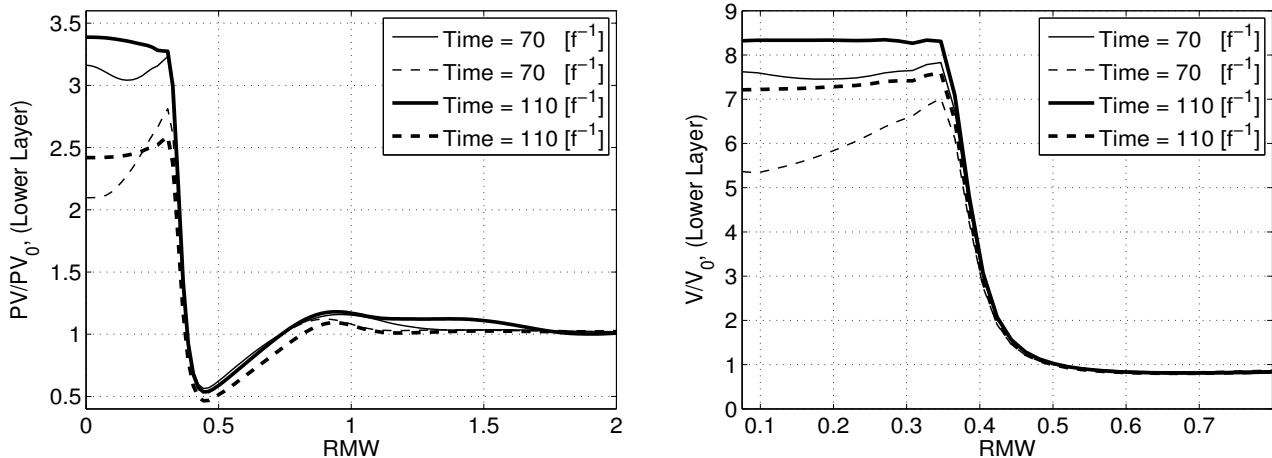


Figure 8. Radial distribution of azimuthally averaged PV (left panel) and velocity (right panel) illustrating the role of the vertical shear in intensification of the vortex. Solid (dashed) lines represent the results of simulations in MCEV environment of the saturation of the instability of BCW (BTW) vortex in the lower layer.

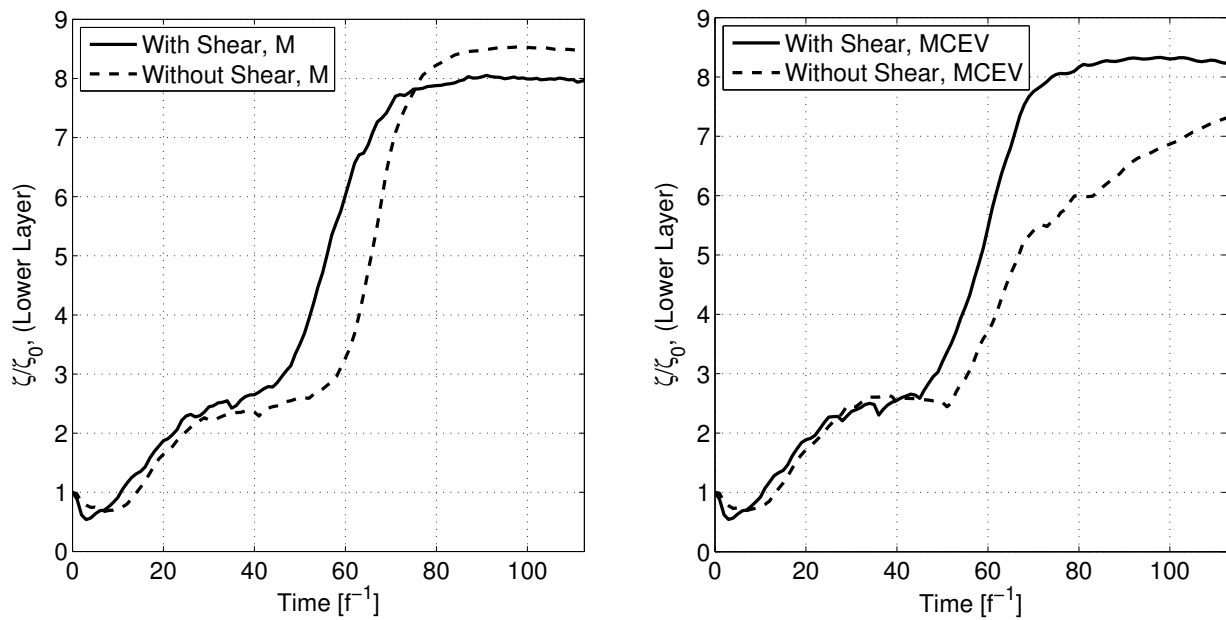


Figure 9. Effect of vertical shear on intensification of vorticity in the vortex core in environments without (M) and with ($MCEV$) moist convection and surface evaporation. The vorticity is normalised by its initial value.

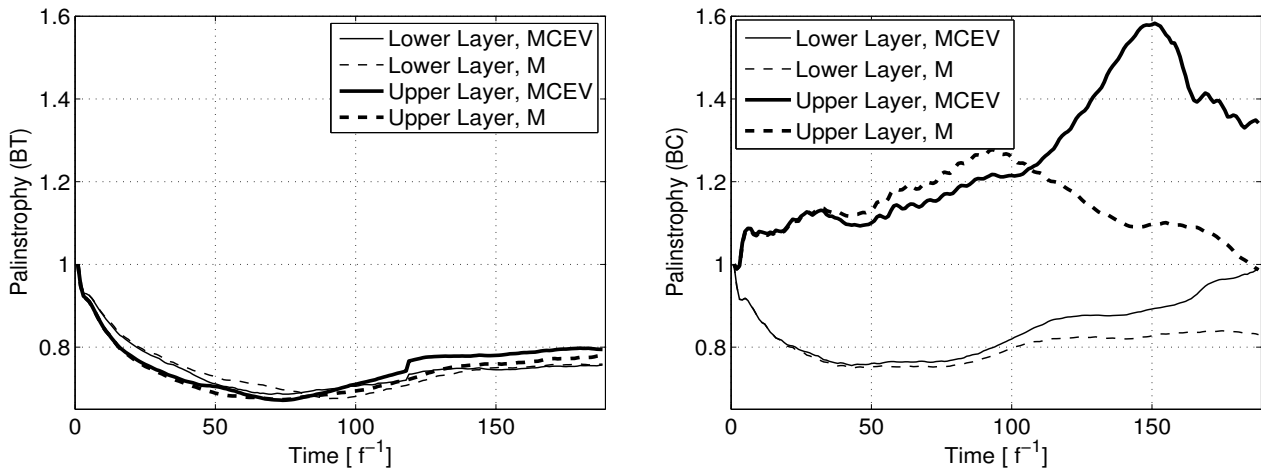


Figure 10. Evolution of palinstrophy in simulations with and without moist convection and surface evaporation of developing instability of the barotropic (left panel) and baroclinic (right panel) cyclones.

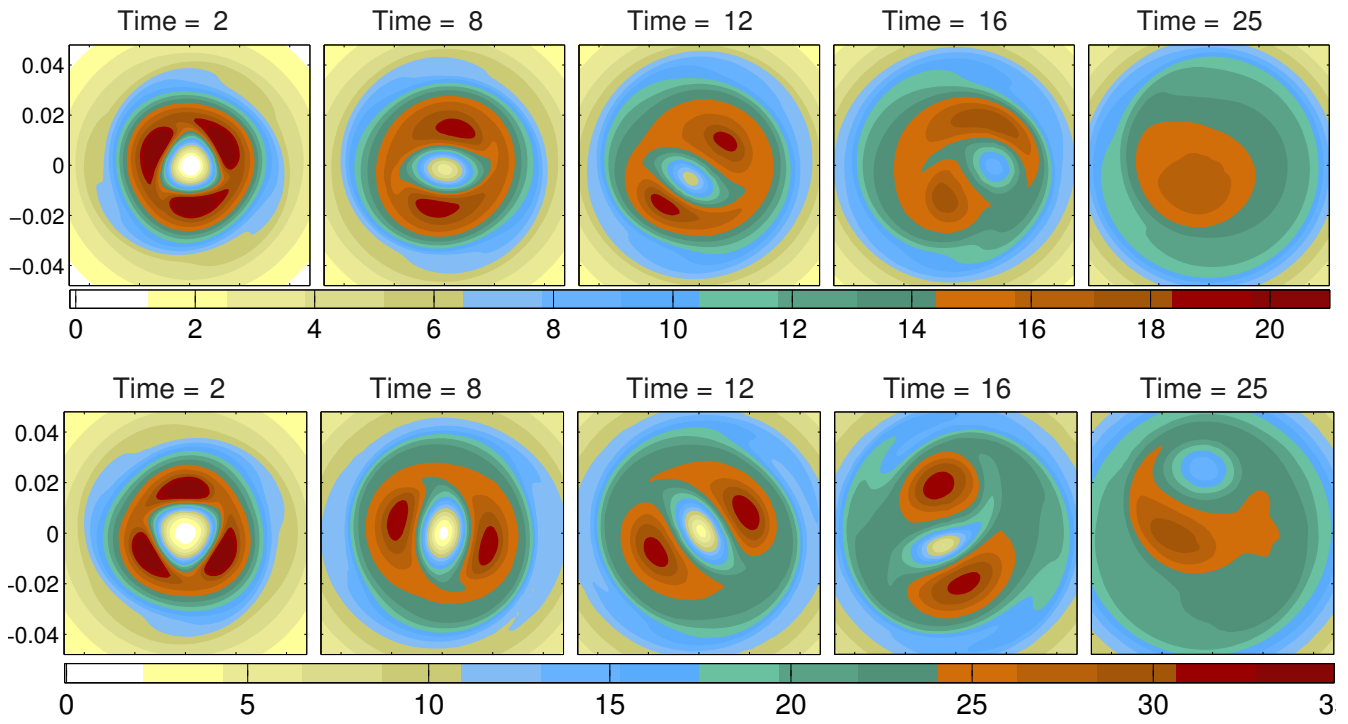


Figure 11. PV evolution during the saturation of $l = 3$ instability of the BCS vortex. Upper (lower) panel: lower (upper) layer.

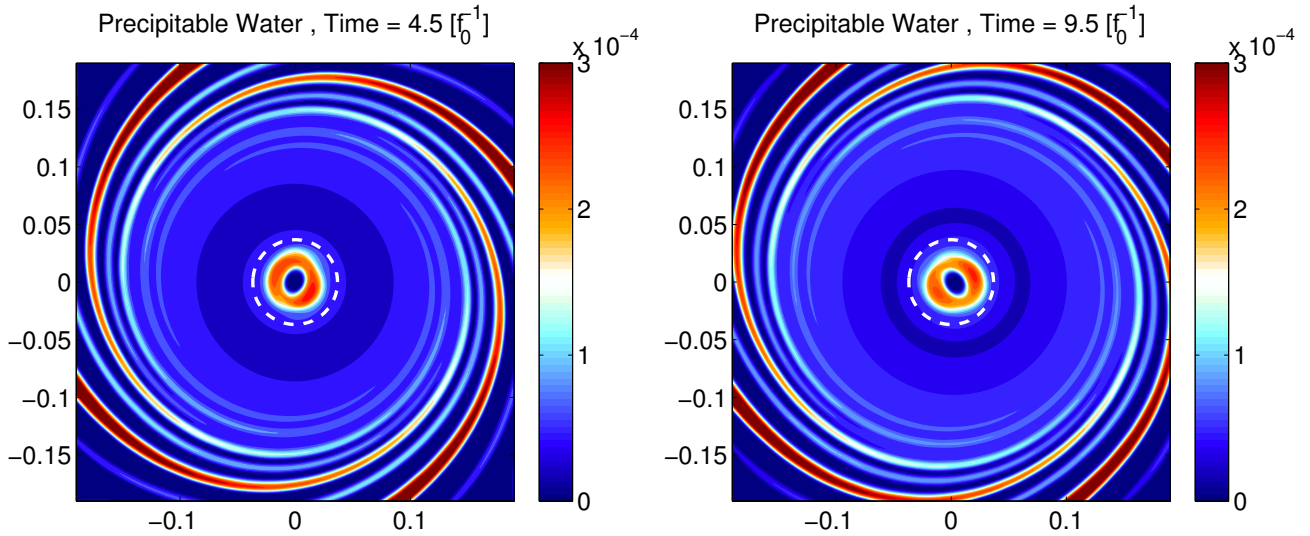


Figure 12. Snapshots of precipitable water during the evolution of the BCS vortex displaying formation of inner and outer spiral bands in the lower layer. Thick dashed line represents RMW. Uniform distribution of initial Q is $Q^s = 0.005$.

Although we limited ourselves above by an application to tropical cyclones, the model can be used for analysis of various phenomena in mid-latitudes and tropics. The passage to the equatorial beta-plane is straightforward in the model, and it can be easily extended to the whole sphere. An important advantage of the model is that it allows for self-consistent inclusion of topography in the numerical scheme, giving a possibility to study a combination of moist and orographic effects. As was already mentioned, more realistic parametrisations of the boundary layer are available, and generalisations to three-layer versions are straightforward.

285 **References**

286 Bouchut, F., Lambaerts, J., Lapeyre, G., Zeitlin, V., 2009. Fronts and nonlinear waves in a simplified shallow-water model of the atmosphere with moisture and
287 convection. *Physics of Fluids* 21 (11), 116604.

288 Guinn, T. A., Schubert, W. H., 1993. Hurricane spiral bands. *Journal of the Atmospheric Sciences* 50 (20), 3380–3403.

289 Hendricks, E. A., Schubert, W. H., 2010. Adiabatic rearrangement of hollow pv towers. *Journal of Advances in Modeling Earth Systems* 2 (4), n/a–n/a, 8.

290 Hendricks, E. A., Schubert, W. H., Chen, Y.-H., Kuo, H.-C., Peng, M. S., 2014. Hurricane eyewall evolution in a forced shallow-water model. *Journal of the
291 Atmospheric Sciences* 71 (5), 1623–1643.

292 Hoskins, B. J., Bretherton, F. P., 1972. Atmospheric frontogenesis models: Mathematical formulation and solution. *Journal of the Atmospheric Sciences* 29 (1),
293 11–37.

294 Kuo, H.-C., Williams, R. T., Chen, J.-H., 1999. A possible mechanism for the eye rotation of typhoon herb. *Journal of the Atmospheric Sciences* 56 (11),
295 1659–1673.

296 Kurihara, Y., 1976. On the development of spiral bands in a tropical cyclone. *Journal of the Atmospheric Sciences* 33 (6), 940–958.

297 Lahaye, N., Zeitlin, V., 2015. Centrifugal, barotropic and baroclinic instabilities of isolated ageostrophic anticyclones in the two-layer rotating shallow water
298 model and their nonlinear saturation. *Journal of Fluid Mechanics* 762, 5–34.

299 Lahaye, N., Zeitlin, V., 2016. Understanding instabilities of tropical cyclones and their evolution with a moist-convective rotating shallow-water model. *Journal
300 of the Atmospheric Sciences* 73, 505–523.

301 Lambaerts, J., Lapeyre, G., Zeitlin, V., 2012. Moist versus dry baroclinic instability in a simplified two-layer atmospheric model with condensation and latent
302 heat release. *Journal of the Atmospheric Sciences* 69 (4), 1405–1426.

303 Lambaerts, J., Lapeyre, G., Zeitlin, V., Bouchut, F., 2011. Simplified two-layer models of precipitating atmosphere and their properties. *Physics of Fluids* 23,
304 046603.

305 Lewis, B. M., Hawkins, H. F., 1982. Polygonal eye walls and rainbands in hurricanes. *Bulletin of the American Meteorological Society* 63 (11), 1294–1301.

306 Mallen, K. J., Montgomery, M. T., Wang, B., 2005. Reexamining the near-core radial structure of the tropical cyclone primary circulation: Implications for
307 vortex resiliency. *Journal of the Atmospheric Sciences* 62 (2), 408–425.

308 Menelau, K., Shecter, D., Yau, M., 2016. On the relative contribution of inertia-gravity wave radiation to asymmetric instabilities in tropical cyclone-like vortices.
309 *Journal of the Atmospheric Sciences* 73, 3345–3370.

310 Montgomery, M. T., Kallenbach, R. J., Jan. 1997. A theory for vortex Rossby-waves and its application to spiral bands and intensity changes in hurricanes.
311 *Quarterly Journal of the Royal Meteorological Society* 123, 435–465.

312 Muramatsu, T., 1986. The structure of polygonal eye of a typhoon. *Journal of the Meteorological Society of Japan. Ser. II* 64 (6), 913–921.

313 Naylor, J., Shecter, D., 2014. Evaluation of the impact of moist convection on the development of asymmetric inner core instabilities in simulated tropical
314 cyclones. *Journal of Advances in Modeling Earth Systems*, 1027–1048.

315 Ooyama, K., 1969. Numerical simulation of the life cycle of tropical cyclones. *Journal of the Atmospheric Sciences* 26 (1), 3–40.

316 Rostami, M., Zeitlin, V., 2017. Influence of condensation and latent heat release upon barotropic and baroclinic instabilities of vortices in a rotating shallow
317 water f-plane model. *Geophysical & Astrophysical Fluid Dynamics* 111 (1), 1–31.

318 Rostami, M., Zeitlin, V., Spiga, A., 2017. On the dynamical nature of saturn's north polar hexagon. *Icarus* 297, 59 – 70.

319 Schecter, D. A., Dunkerton, T. J., 2009. Hurricane formation in diabatic ekman turbulence. *Quarterly Journal of the Royal Meteorological Society* 135 (641),
320 823–838.

321 Schubert, W. H., Montgomery, M. T., Taft, R. K., Guinn, T. A., Fulton, S. R., Kossin, J. P., Edwards, J. P., 1999. Polygonal eyewalls, asymmetric eye contraction,
322 and potential vorticity mixing in hurricanes. *Journal of the Atmospheric Sciences* 56 (9), 1197–1223.

323 Stevens, B., Bony, S., 2013. What climate models miss? *Science* 340, 1053.

324 Wang, Y., 2009. How do outer spiral rainbands affect tropical cyclone structure and intensity? *Journal of the Atmospheric Sciences* 66 (5), 1250–1273.

325 Willoughby, H. E., 1978. A possible mechanism for the formation of hurricane rainbands. *Journal of the Atmospheric Sciences* 35 (5), 838–848.

326 Zeitlin, V., 2008. Decoupling of balanced and unbalanced motions and inertia - gravity wave emission: Small versus large rossby numbers. *Journal of the
327 Atmospheric Sciences* 65, 3528–3542.

328 Zhong, W., Zhang, D. L., 2014. An eigenfrequency analysis of mixed rossby-gravity waves on barotropic vortices. *Journal of the Atmospheric Sciences* 71,
329 2186–2203.

330 Zhong, W., Zhang, D. L., Lu, H., 2009. A theory for mixed rossby-gravity waves in tropical cyclones. *Journal of the Atmospheric Sciences* 66, 3366–3381.